



HAL
open science

Ultrafast electronic relaxations from the S3 state of pyrene

Jennifer A. Noble, Christian Aupetit, Dominique Descamps, Stephane Petit, Aude Simon, Joëlle Mascetti, Nadia Ben Amor, Valérie Blanchet

► **To cite this version:**

Jennifer A. Noble, Christian Aupetit, Dominique Descamps, Stephane Petit, Aude Simon, et al.. Ultrafast electronic relaxations from the S3 state of pyrene. *Physical Chemistry Chemical Physics*, 2019, 21 (26), pp.14111-14125. 10.1039/C8CP06895J . hal-02073683

HAL Id: hal-02073683

<https://hal.science/hal-02073683>

Submitted on 30 Aug 2022

HAL is a multi-disciplinary open access archive for the deposit and dissemination of scientific research documents, whether they are published or not. The documents may come from teaching and research institutions in France or abroad, or from public or private research centers.

L'archive ouverte pluridisciplinaire **HAL**, est destinée au dépôt et à la diffusion de documents scientifiques de niveau recherche, publiés ou non, émanant des établissements d'enseignement et de recherche français ou étrangers, des laboratoires publics ou privés.

Cite this: DOI: 10.1039/xxxxxxxxxx

Ultrafast electronic relaxations from the S_3 state of pyrene.

Jennifer A. Noble,^{a†} Christian Aupetit^a, Dominique Descamps^b, Stéphane Petit^b, Aude Simon^c, Joelle Mascetti^a, Nadia Ben Amor^c and Valérie Blanchet^{†b}

Received Date

Accepted Date

DOI: 10.1039/xxxxxxxxxx

www.rsc.org/journalname

The ultrafast relaxation occurring in pyrene upon excitation at 4.68 eV was studied in a supersonic gas-jet fs pump-probe experiment. Mass spectrometry and velocity map imaging of photoelectrons produced by probing via multiphoton ionisation at 800 nm reveal that the initially prepared wave packet exhibits a fast relaxation (<80 fs), followed by a slower one of 200 fs. By comparing the propensity rules of photoionisation observed at one color with *ab initio* calculations, we tentatively assign these two timescales to a first internal conversion to the dark bB_{3g} state followed by a second one to the long lived aB_{2u} first excited state. Vertical excitation energies determined using *ab initio* Multi-State Complete Active Space 2nd order Perturbation Theory (MS-CASPT2), as well as oscillator strengths between several electronic states, are reported.

1 INTRODUCTION

Polycyclic aromatic hydrocarbons (PAHs) are widespread atmospheric pollutants, produced by natural processes, such as forest fires, as well as by human activities, such as combustion of fossil fuels^{1,2}. During their lifetimes in the troposphere, they may undergo UV-visible photochemical degradation, forming harmful by-products such as nitro-, hydroxy-, or oxo- PAH compounds upon reaction with other molecules or radicals (e.g. NO_x , SO_x , OH, H_2O , or O_3 ³). Additionally, PAHs are thought to be ubiquitous in the interstellar medium (ISM), where they account for up to 10-20 % of the cosmic carbon budget in the galaxy^{4,5}. Despite the fact that no individual PAH molecule has yet been identified, a population of PAHs is believed to be responsible for a series of emission features observed between 3 and 20 μm in the ISM, known as the aromatic infrared bands (AIBs⁶). Upon irradiation by VUV photons in certain interstellar environments, PAHs undergo ionisation and fragmentation processes⁷ and,

based upon the results of laboratory experiments, it is expected that they will undergo additional photoreactions with abundant species such as H_2 , H_2O , H, or OH (see for instance, the work by Andrews *et al.*⁸ or Cook *et al.*⁹). In photodissociation regions (PDRs), spatial variations in the IR emission spectra have been attributed to differences in the charge (neutral or cationic) of PAH classes^{10,11}, and it is important that these are integrated into astrophysical models of such regions. It is therefore valuable to study the photophysics of PAHs over a wide frequency range in order to understand their photochemistry in different environments.

In the present work, we have chosen the molecule of pyrene as a model of pericondensed PAH of both atmospheric and astrochemical interest¹². Ultrafast relaxation in cold, gas-phase PAHs has been studied for neutral azulene¹³, as well as the parent cations of naphthalene, pyrene, and tetracene¹⁴. This work is a follow-up study on pyrene, in which we target the third optically allowed excited state (S_3), lying at ~ 4.68 eV above the ground state S_0 . The most advanced gas phase electronic study of neutral pyrene produced a fluorescence excitation spectrum of jet-cooled pyrene that reveals very broad bands for the S_3 and S_4 states¹⁵. More is known about the cation, whose electronic structure is used here as a continuum sensitive to changes of electronic configurations and sometimes to vibrational dynamics. Pyrene is a pericondensed PAH in which a high degree of photoionisation can be reached more easily than in catacondensed PAHs^{16,17}. PAHs typically absorb around 10^8 UV photons over their lifetime in the ISM¹⁸. The competition between the different relaxation paths – i.e. ionisation or dissociation – after absorption of UV-photons

^aUniversité de Bordeaux-CNRS, ISM, F33405 Talence, France

^bUniversité de Bordeaux-CNRS-CEA, CELIA, UMR5107, F33405 Talence, France

^cUniversité de Toulouse-CNRS-UT3, LCPQ-IRSAMC, F-31062 Toulouse, France

[†]Present address : Aix-Marseille Université-CNRS, PIIM, 13397, Marseille, France

† Electronic Supplementary Information (ESI) available:

Figure S1: Triply charged Pyrene

Figure S2: Photoelectron images at three different pump probe delays

Table S1: Optimized B3LYP geometries

Table S2: C-C distances in the B3LYP geometries

Table S3: Non adiabatic coupling

Figure S3: CASSCF Molecular Orbitals

Table S4: Excitation energies and oscillator strengths between excited states

Table S5: Dyson orbitals

See DOI: 10.1039/cXCP00000x/

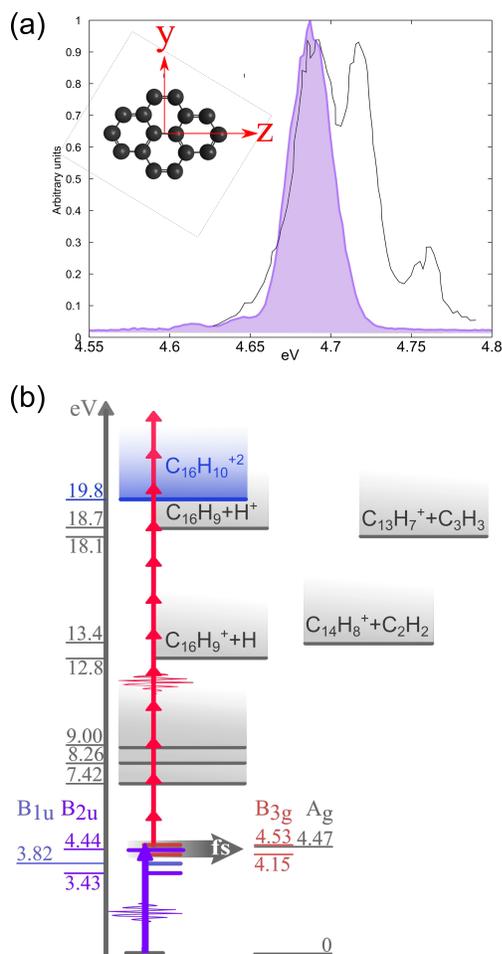


Fig. 1 Excitation scheme with (a) the absorption spectrum extracted from ¹⁵ and the pump spectrum (purple plot) used in the present experiment, and (b) a schematic summarizing the excited states of neutral pyrene calculated by MS-CASPT2 (with one different color for each electronic symmetry) as well as the first three cation states and the thresholds for dissociative ionisation. See Table 1 and Table 4 for details.

is a key question for astrochemistry. Indeed, after the absorption of a UV photon, electronic excited states can be populated, leading to omnipresent successive internal conversions, followed by intramolecular vibrational relaxation and eventually dissociation. These relaxations will have an impact on the branching ratio observed in photoionisation. Table 1 summarises the dissociation energies calculated from the appearance energies.

The remainder of the paper is structured as follows. In Section 2 we describe the femtosecond pump-probe experiment using a velocity map imaging (VMI) spectrometer. In Section 3 we present the mass spectra recorded at three different pump-probe delays, as well as the corresponding ion and photoelectron transients. In Section 5, we discuss the results in the context of *ab initio* calculations presented in Section 4, before summarising our conclusions.

2 EXPERIMENTAL SET-UP

The experimental setup consists of a molecular beam chamber with a 1 kHz Even-Lavie pulsed valve, coupled to a VMI spec-

trometer and a 25 fs, 1 kHz, Ti:Sapphire laser system (Aurore – 800 nm). One part of the laser beam is used to generate the pump pulse at ≈ 4.68 eV (≈ 265 nm) with a 30 meV Full Width Half Maximum (FWHM), *i.e.* 60 fs Fourier limited pulse. This pump pulse is produced by summing the second harmonic at 400 nm (produced in 200 μm -BBO crystal) with the fundamental pulse via a second BBO crystal of 150 μm thickness. To photoionise pyrene, $\text{C}_{16}\text{H}_{10}$, whose adiabatic ionisation potential is $\text{IP}_a = 7.4256 \pm 0.0006$ eV²¹, the probe pulse is simply the fundamental pulse centered at 1.55 eV with a 100 meV FWHM. In this experiment, it was not possible to get a pump-probe contrast on the ions with the second harmonic used as a probe, as will be discussed further below. The pump and probe pulses are linearly polarised, parallel to each other and parallel to the detector, in order to maintain the required cylindrical symmetry for the photoelectron imaging. The pump and probe pulses are focused with 230 mm and 320 mm thin lenses, respectively. The pump energy is set relatively low at 10 $\mu\text{J}/\text{p}$ and focused 1 cm away from the 3 mm molecular beam for all the experimental results presented here. This restrains the intensity to 7×10^{10} W/cm², in order to avoid multiphoton absorption of the pump that is the main source of background signal. The probe intensity (60 $\mu\text{J}/\text{p}$) with a measured 170 μm beam waist focused on the molecular jet, reaches 2×10^{12} W/cm² in order to get sufficient pump-probe contrast. The ponderomotive down-shift of the potential ionisation threshold – that is the cycle-averaged quiver energy of a free electron in the 800 nm intense field – is expected around 130 meV, depending on the quality of the NIR (Near Infra Red) spatial mode. The time-overlap and the time-resolution were both determined by photoionisation of acetone²⁴, produced at room temperature through a bubbler with a He carrier gas (10 bar). Prior to recording any time-transients of pyrene, a deep pumping of the gas lines was done to remove any contamination from the acetone on the mass spectra.

Pyrene (Sigma-Aldrich, 98 % purity) was introduced into the chamber via a pulsed Even-Lavie valve with a 250 μm conical nozzle. The valve was heated to 105 °C to ensure sufficient vapour pressure and to avoid cluster formation when pyrene was introduced in conjunction with the minimal 10 bars of Helium required to get a stable pulsed molecular beam. The photoelectrons or photoions produced upon irradiation are extracted in a direction perpendicular to the plane defined by the laser and molecular beams, and detected at the end of a 40 cm time-of-flight tube using an imaging detector consisting of two micro-channel plates (MCP, 7 cm diameter) coupled to a phosphor screen (P43) and a 12 bit CCD camera. On the ion images, there is no trace of cluster formation (which would appear at higher distance from the center of the detector due to their higher masses), nor of pyrene cations resulting from cluster dissociation (with velocity vectors perpendicular to the molecular beam axis). The mass spectra are collected from the phosphor plate, preamplified ($\times 200$) and averaged over 10k sweeps on a 4 GHz oscilloscope. The transient ion signals are recorded using gated boxcar integrators. Taking into account the large background observed on the pyrene cation, the pump-probe photoelectron images can not be used as is. At

Table 1 Dissociation and ionisation energies for various channels, in both absolute values and the relative energies from the ground state of the neutral parent. All the energies are vertical energies except the † measurement.

Channel	Ion amu/q	Energy in eV	Energy from S ₀	Determination	Ref.
Dissociation/Fragmentation					
C ₁₆ H ₉ + H	-	4.7	<i>idem</i>	DFT	16
C ₁₄ H ₈ + C ₂ H ₂	-	6.9	<i>idem</i>	DFT	16
C ₁₆ H ₉ ⁺ + H	201	5.4 ± 1.2	12.8	exp	19
		5.1	12.5	DFT	19
C ₁₄ H ₈ ⁺ + C ₂ H ₂	176	6.02	13.44	DFT	19
C ₁₅ H ₉ ⁺ + CH	188	7.1	14.52	DFT	20
C ₁₃ H ₇ ⁺ + C ₃ H ₃	163	10.67	18.09	DFT	20
C ₁₆ H ₉ + H ⁺		11.3	18.3 or 18.7	DFT	16
C ₁₄ H ₈ + C ₂ H ₂ ⁺	26	11	18.5	DFT	16
Ionization					
C ₁₆ H ₁₀ ⁺ (D ₀) + e ⁻	202	7.4256 ± 0.0006†	<i>idem</i>	exp.	21
D ₀		7.415 ± 0.01	<i>idem</i>	exp.	22
D ₀		7.44	<i>idem</i>	MS-CASPT2	this work
D ₁		8.26		exp.	23
		8.29	<i>idem</i>	MS-CASPT2	this work
D ₂		9.00		exp.	23
		9.02	<i>idem</i>	MS-CASPT2	this work
C ₁₆ H ₁₀ ²⁺ + 2e ⁻	202/2 ~ 101	19.8 ± 0.2	<i>idem</i>	exp.	22
C ₁₆ H ₁₀ ²⁺		19.24	<i>idem</i>	MS-CASPT2	this work
C ₁₆ H ₁₀ ³⁺ + 3e ⁻	202/3 ~ 67	36.44	<i>idem</i>	exp.	16

each delay, two background images of 10k laser shots each, corresponding to only the pump (“Pump alone”) and only the probe (“Probe alone”) pulses are recorded and subtracted (with the appropriate weighting) from the pump-probe photoelectron image recorded over 40k laser shots. The pump-probe delays are then scanned twelve times. This allows the collection of statistically significant data for the subtracted pump-probe images recorded over 480k laser shots. The photoelectron images are then Abel inverted in order to reconstruct the 3D photoelectron distributions and to extract the kinetic energy and angular distributions of the photoelectrons. The energy resolution of 0.25 eV for a 3 eV photoelectron kinetic energy and calibration are both determined from the photoionisation of argon using the same optical set-up.

3 EXPERIMENTAL RESULTS

In pyrene, the 1+2’ total energy reaches the ion continuum at only 360 meV above the IP_a, while the various dissociative ionisation thresholds require higher multiphotonic order of NIR. This excitation scheme is summarised in Figure 1; also shown is the absorption spectrum of the S₃ band, reproduced from¹⁵.

Figure 2 shows the mass spectra recorded at -250 fs (first interaction with the NIR pulse), 0 fs, and 250 fs (first interaction with the UV pulse). These spectra are dominated by the parent molecular ion (202 amu) and the well established dissociative ionisation channels from -H up to -4H losses observed in multiphoton ionisation,^{25,26} due to the fact that all H atoms in PAHs have similar binding energies²⁷. Apart from these main peaks, the second most intense pattern appears around mass 101. The presence of several peaks around 202/(q=2) amu leads us to assign this set to doubly ionised parent molecules, as has previously

been observed both in fs multiphoton ionisation at 800 nm²⁵ and in ion beam collision²⁸. At the pump-probe time-overlap, multicharged ionisation is so efficient that the triple ionisation continuum is reached (shown in the ESI†, Figure S1). The triply charged molecules are formed by the pump-probe ionisation and survive the 7 μs of the time-of-flight, suggesting a rarely observed stability for a triply charged species. It is, indeed, well-known that pericondensed PAHs do not fragment easily after photoelectron emission and it has even been calculated that pyrene becomes thermodynamically unstable once the charge q ≥ 4¹⁶. With a significantly smaller probability, the -C₂H₂ loss peaks appear, as expected, among the dissociative channels at the lowest energy (see Table 1). It should be noted that, once the doubly charged ion continuum is energetically opened, dissociative ionisation is in play, with even the -CH loss channel detected. The most important point for the following discussion is that this mass spectrum reveals that most of the photoelectrons detected will be produced in coincidence with pyrene cations.

Figure 3 shows the transients recorded on the main ion peaks, *i.e.*, the cation of pyrene (202 amu), its dication (202/2 amu), and the proton. Also worth noting is the large background observed on the C₁₆H₁₀⁺ transient, mainly produced by the pump pulse alone (see the inset), while on the dication transient, the main background is produced by the probe pulse alone. This weak pump-probe contrast observed on C₁₆H₁₀⁺ transient, despite an off-focused pump pulse, requires the careful background subtraction of the time-resolved photoelectron spectroscopy (TR-PES), as will be discussed further below. This efficient UV absorption cross-section also explains why, in the femtosecond regime, a UV+403 nm pump-probe scheme does not lead to any tran-

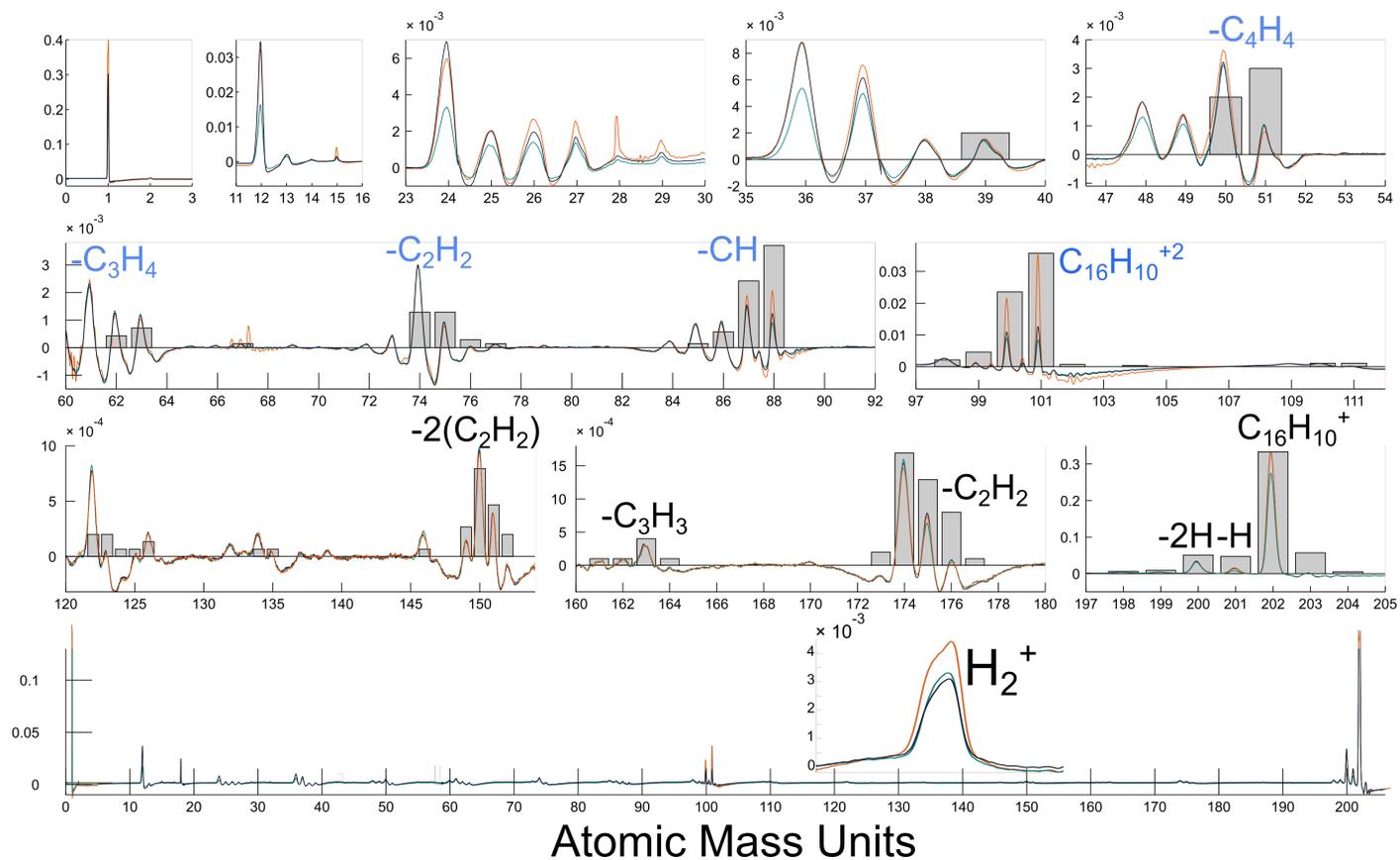


Fig. 2 The mass spectra obtained at -250 fs (green), 0 fs (orange), and +250 fs (black) compared to the electron ionisation mass spectra (grey bars, NIST). No carrier gas He^+ is detected. Only the main masses including 202, 101, and 1 amu were recorded as a function of the pump-probe delay. A magnification of the triply charged pyrene is presented in the ESI† (Figure S1).

sient with a proper contrast: the UV pump-UV probe contribution is buried in two large background signals, one produced by the 264.7 nm alone and the second one by the 403 nm (resonant at 6.2 eV).

Fits of the pyrene transients were made by convolving the standard single-exponential decaying function with an instrumental error function in which the main parameters (the cross-correlation time τ_{cc} and the 0 fs time-overlap) are provided by the acetone gaussian trace:

$$S_{ion}(t) = y_0 + a \times e^{-\frac{t-t_0}{\tau_d}} \times [1 + \text{erf}(\phi(\tau - t_0, \tau_d))] \quad (1)$$

where y_0 is a background signal, τ_d the decay time to extract, and t_0 a timeshift that is required for the pyrene cation and some photoelectron components. For the proton transient, a second decay was required. The component in the error function is expressed by:

$$\phi(\tau, \tau_d) = \frac{2\sqrt{\ln 2}}{\tau_{cc}} \times \left(\tau - \frac{\tau_{cc}^2}{8\ln 2 \times \tau_d} \right)$$

The time-dependencies extracted from these fits are all summarised in Table 2. The values of t_0 reveal mainly the first internal conversion whereas the decays τ_d result from either a second internal conversion or an intramolecular vibrational relaxation (IVR), as will be discussed further below.

Figure 4 presents the one-colour photoelectron spectra (PES) recorded at 264.7 nm (0.1M laser shots, panel a), 800 nm (1.2M laser shots, panel b), and 403 nm (0.8M laser shots, panel c). Taking into account the pulse duration of these three colours and in combination with *ab initio* calculations (see Section 4), these one-colour photoelectron spectra can help to identify the propensity rules of the photoionisation at play in electronically excited pyrene. Indeed, for photoionisation taking place at ~ 9.4 eV, the emission of the outer electron occurs, in general, without simultaneous electronic reorganisation of the cation. The simplest correlation revealed by one-photon ionisation is then the cation states formed from the removal of the outer single active electron of the neutral electronic excited state(s)²⁹. It is this main approximation that will sustain all the reasoning employed to assign the transients presented in this work.

The thresholds of the first three cation states are clearly identified on the resonant 1+1 UV PES at 264.7 nm shown in Figure 4a. This is very similar to that previously reported in smaller PAHs like azulene for fs-UV resonant photoionisation.¹³ There are also some photoelectrons produced above 2 eV kinetic energy, resulting from photoionisation at 3×264.7 nm. In this case, the total energy will be 14 eV, and dissociative photoionisation, producing primarily photoelectrons with low kinetic energies, will be active. This UV PES has been fitted in order to retrieve the relative contributions of the first three states of the ions. All contributions have been fitted by a $(1 - \text{erf}((E - E_i)/\Delta E))$ function with E_i fixed at the expected kinetic energies for threshold ionisation, *i.e.* 1.95, 1.12, and 0.32 eV for D_0 , D_1 , and D_2 , respectively. ΔE is fixed to be the same for all the 2×264.7 nm contributions, and is found to be 170 ± 20 meV, whereas ΔE is found to be 1.12 ± 0.29 eV for the

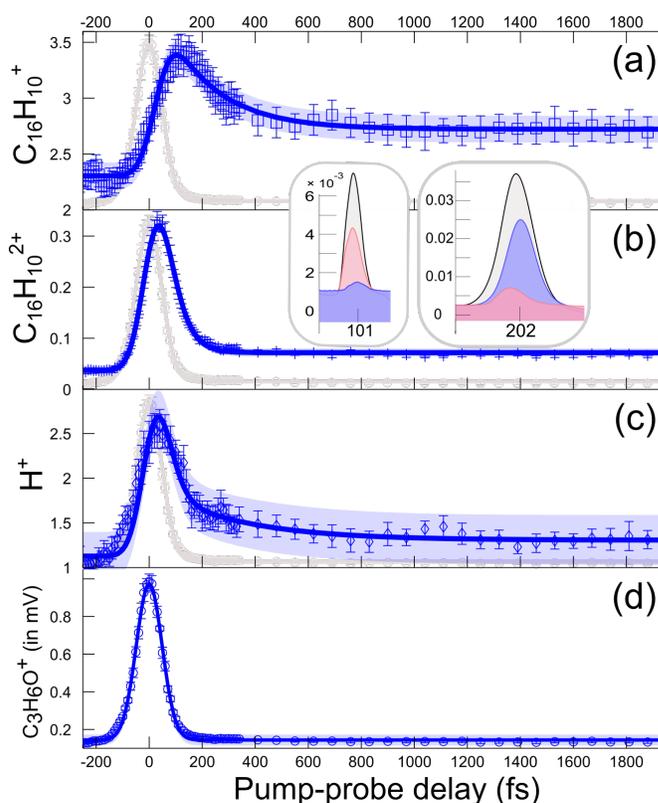


Fig. 3 Pump-probe transients on (a) the pyrene cation, (b) the doubly ionised pyrene dication, (c) the H^+ fragment, and (d) the acetone cation used to determine the 0 fs time-overlap and the cross-correlation time τ_{cc} . The acetone trace is shown on each transient to emphasise the t_0 shifts observed, as well as the time resolution of the instrumental function. The y-scale is an arbitrary unit that maintains the relative yields of the cations. The vertical uncertainties are obtained from the successive ion scans, while the blue areas mark the 50 % confidence level in the fits. All time constants extracted from the fits are listed in Table 2. The two insets show the mass spectra with the pump alone (blue area), the probe alone (red area), and the pump-probe at 100 fs (grey area) for the pyrene cation (202 amu) and the dication (202/2 amu).

3×264.7 nm PES. This large contribution results from the strong dissociative ionisation yielding slow photoelectrons. Based on these UV PES fits, the 3× 264.7 nm reaches 30 % ± 10 %, while at 2×264.7 nm, the branching rates are: 31 % ± 4 %, 51 % ± 5 %, and 18 % ± 2 % for D₀, D₁, and D₂, respectively.

The multiphoton ionisation at 800 nm (with a minimum of n=5 photons to reach IP_a) reveals a comb of above-threshold ionisation (ATI) built on D₀ as seen in Figure 4b (indicated by grey lines for n=6–8). Based on the rare gas calibration done with the UV alone, the ponderomotive shift induced by the 800 nm intensity was measured as 65 meV, *i.e.* two times smaller than the expected value, attributable to the quality of the spatial mode of the probe pulse. To aid the reader, this ponderomotive shift to higher kinetic energy has been corrected for in the x axis of Figure 4b. Three additional peaks are observed on top of the ATI comb between 0.5 and 1.05 eV (marked with blue lines in Figure 4b). Multiphoton ionisation at 800 nm at the threshold of D₁ will produce a photoelectron with 1.05 eV kinetic energy. The two extra features that appear at 0.56 and 0.87 eV (blue dotted and dashed lines) can be assigned to vibrational activity in the D₁ ion continuum, as has previously been observed upon VUV ionisation into D₀.²² Their corresponding quantum energies are 175 meV and 485 meV. While the first one is in good agreement with the a_g CC stretching quantum at $\nu_{CC}=1389\text{ cm}^{-1}$ (172 meV)^{22,30}, the second is larger than the $\nu_{CH}=3077\text{ cm}^{-1}$ (381 meV-b_{2u}) aromatic-CH stretching quantum^{31,32}. However, when combined with the longitudinal stretching mode in the plane of the molecular skeleton, ν_{LS} with a quantum of 402 cm⁻¹ (50 meV),^{22,33} the photoelectron peaks would be expected to lie at 0.62 eV and 0.57 eV for $\nu_{CH}+\nu_{LS}$ and $\nu_{CH}+2\times\nu_{LS}$, respectively. Infrared spectroscopy of gas phase cations created by electron impact has also revealed significant activity around 11.83 μm, corresponding to an out-of-plane bending mode ($\nu_{OB}=847\text{ cm}^{-1}$).¹² With the current resolution of the VMI, it is not possible to distinguish 2 ν_{LS} (at 804 cm⁻¹) from one quanta of ν_{OB} . What is important to note for what follows is that in the multiphoton ionisation onto D₁ from the equilibrium geometry of S₀, ν_{CH} does not appear on its own, contrary to ν_{CC} .

Multiphoton ionisation at 800 nm is enhanced by resonances at 4.65 eV – *i.e.* the same state reached at 264.7 nm – as well as resonance(s) around 6.2 eV. In this context, it is relevant to also photoionise at 403 nm, for which the first resonance encountered is also reached around 6.2 eV (2×403 nm). This 403nm-PES (Figure 4c) is characterised by a shoulder at 1.82 eV and three large contributions at 1.41 eV, 0.98 eV, and 0.61 eV. At the thresholds of the first three cation states, photoelectrons should be emitted with kinetic energies of 1.81, 0.98, and 0.18 eV (solid lines, Figure 4c). If one ν_{CH} quantum is populated into D₀ and D₁, the kinetic energies are reduced to 1.43 and 0.60 eV (dashed lines), respectively. In conclusion, the 6.16 eV-enhanced photoionisation seen in Figure 4c also reveals photoionisation into D₀ and D₁ with activity in the CH stretching mode on its own.

In azulene, in naphthalene, and also in coronene, the

multiphoton-ionisation was mainly characterised by Rydberg fingerprints.^{13,34,35} These fingerprints result from doubly excited states reached at intermediate energies in the multiphoton ionisation and that decay over a duration shorter than the probe duration to Rydberg states. The PES is then dominated by photoionisation taking place from the Rydberg states with a $\Delta\nu = 0$ propensity rule. Table 4 shows the presence of several states in the 5-6.3 eV range that are partly characterised by the creation of two holes. In order to check our assignment and to detect the possible contribution of Rydberg fingerprints, we have also recorded PES at 405 nm. The PES has exactly the same pattern as at 403 nm but shifted by 45 meV (three times the energy difference of 403 nm and 405 nm) and not by 15 meV as would be expected if a Rydberg fingerprint was at play around 6.2 eV.¹³ From Figure 4, we conclude that only 2×264.7nm enhanced-ionisation populates the D₂ ion continuum while only resonant multiphoton ionisation with the short pulses (<30 fs) centered at 800 nm and at 403 nm imprints vibrational activities onto the PES.

The angular distributions of the photoelectrons, shown in the insets of Figure 4, are fitted at the kinetic energies of interest by $I(\theta) = 1 + \sum \beta_n \times P_n(\cos(\theta))$, with $P_n(x)$ being the Legendre polynomials. The extracted β_n parameters are listed in Table 3. For the 264.7 nm ionisation, the angular distributions of D₁ and D₂ are quite isotropic with β_2 values close to zero. This is similar to what was previously recorded on azulene using resonant-UV photoionisation, producing photoelectrons preferentially along the axis of the TOF despite a laser polarisation parallel to the molecular beam.¹³ Via the resonances reached around 6.2 eV at 2×403 nm, the angular dependency starts to be slightly anisotropic, with β_2 reaching almost 2 for D₀ at threshold. The multiphoton ionisation at 800 nm strongly selects the molecular orientation, resulting in β_2 close to 2 and requiring higher orders of the Legendre polynomial to describe the anisotropies.

Figure 5 presents the time-dependencies of the background-subtracted photoelectron spectrum. Three Abel inverted images, measured at the principal delays of interest, are shown in ESI† (Figure S2). The angular dependencies, summarised in Table 3 are significantly more anisotropic than the ones observed at 2×264.7nm, possibly due to the resonances reached at 6.23 eV in the multiphoton probe step. In the pump-probe photoionisation scheme, only two NIR photons are required to reach the threshold of D₀ (1+2' total energy). However, as seen in Figure 5, up to five NIR photons are absorbed to produce the PES, reaching a total energy of 12.4 eV. To increase the visibility of the time dependencies of all of the photoelectrons < 1.5 eV, the PES recorded at 10 ps is subtracted from all the PES recorded at shorter delays. Indeed, as is evident from the ion transients in Figure 3, we can expect that beyond 2 ps no more electronic relaxations are at play. Figures 5b and 5c show these subtracted TR-PES. The D₂ and D₁ continua are energetically accessible in 1+3', with a maximum kinetic energy of 0.28 and 1.08 eV, respectively. The peaks at 0.9 and 0.52 eV are assigned to D₁+ ν_{CC} and D₁+ $\nu_{CH}+\nu_{CC}$ (blue vertical lines). The first peak

Table 2 Time dependencies (fs) derived from the S_3 state excitation at 4.68 eV.

Signal	Species	Figure	τ_{cc}	τ_d	t_0
IONS	$\text{CH}_3\text{C}(\text{O})\text{CH}_3^+$	3d	114 ± 1	0	0
	$\text{C}_{16}\text{H}_{10}^+$	3a	-	192 ± 11	22 ± 2
	$\text{C}_{16}\text{H}_{10}^{+2}$	3b	-	45 ± 1	0
	H^+	3c	-	29 ± 1	0
		3c	-	318 ± 1	0
PHOTOELECTRONS	$\text{D}_2 + \nu_{CC}$ at ~ 0.13 eV	5e (orange)		280	80
	$\text{D}_1 + \nu_{CC} + \nu_{CH}$ at ~ 0.52 eV	5e (green)		170	80
	$\text{D}_1 + \nu_{CC}$ at ~ 0.9 eV	5e (cyan)		200	80

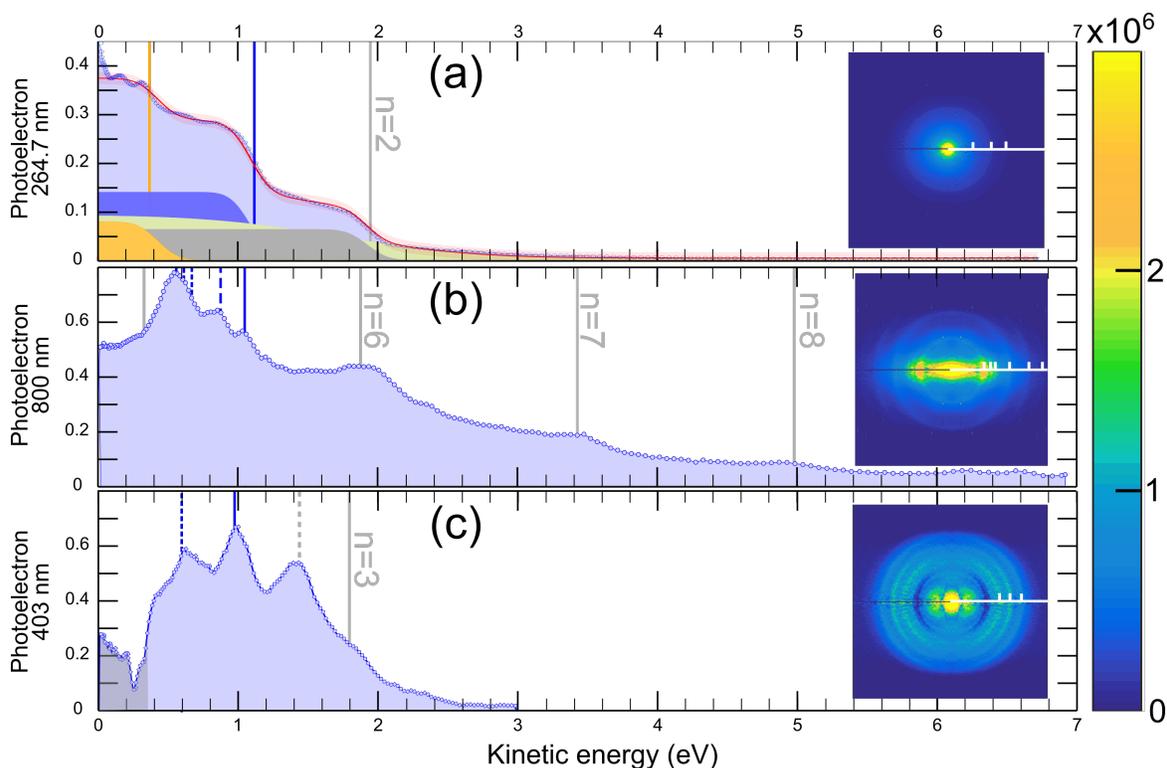


Fig. 4 Normalised one colour photoelectron spectra recorded (a) at 264.7 nm (4.68 eV per photon), labelled with the anticipated kinetic energies of the thresholds of $\text{D}_0=7.42$ eV (grey line), $\text{D}_1=8.26$ eV (blue line), and $\text{D}_2=9.00$ eV (orange line)²². The red area shows the 50 % confidence interval of the PES fit with the different contributions indicated with the same colour code as the vertical lines. The green area is the 3×264.7 nm contribution estimated from the PES fit; (b) at 800 nm (1.55 eV per photon), labelled with the four peaks of ATI build on D_0 (grey lines, $n=5-8$) and vibrational activity in the D_1 cation (blue line) reached at six photons, with the $\nu_{CC} = 1389 \text{ cm}^{-1}$ CC stretching (dashed blue line), as well as a combination of $\nu_{CH}=3077 \text{ cm}^{-1}$ aromatic CH stretching mode+skeletal mode $\nu_{LS}=402 \text{ cm}^{-1}$ or either with out-of-plane bending mode $\nu_{OB} = 850 \text{ cm}^{-1}$ (dotted blue lines). To aid the reader, the energy axis has been down shifted by 65 meV to correct for the ponderomotive shift; (c) at 403 nm (3.08 eV per photon), recorded at a higher resolution by using a lower voltage on the repeller electrode. Employing the same convention as (b), the D_0 and D_1 thresholds are indicated, as well as the ν_{CH} mode in each cation state. The area marked in grey was deeply affected by a lower gain on the detector at that time during the experiment. For each of the three wavelengths, the inset corresponds to an Abel transformation of the VMI image, with Table 3 listing the anisotropy parameter(s) of the angular dependency of each one colour-photoionisation component. Note that $n=2$ at 264.7 nm, $n=6$ at 800 nm, and $n=3$ at 403 nm correspond to photoionisation taking place around 9.3 eV.

Table 3 Photoelectron anisotropies. Fit of the angular dependencies by $I(\theta) = 1 + \sum \beta_n \times P_n(\cos(\theta))$, with $P_2(x) = \frac{1}{2}(2x^2 - 1)$ and $P_4(x) = \frac{1}{8} \times (35x^4 - 30x^2 + 3)$. All the β_2 are listed as well as the β_n coefficients larger than 5% of the β_2 value.

Cation States	264.7nm (Figure 4a)	800nm (Figure 4b)	403nm (Figure 4c)	Pump-probe 216 fs/405 fs/5 ps (ESI† Figure S 2)
D ₀	0.65	$\beta_2=1.91(n=6)/2(n=7), \beta_4=0.32/0.92$	1.8	1.44-1.45-1.55
D ₀ + v_{CH} (3077 cm ⁻¹)	-	-	0.9	
D ₁	0.13	$\beta_2=1.57, \beta_4=0.34$	0.6	
D ₁ + v_{CC} (1389 cm ⁻¹)	-	$\beta_2=1.27, \beta_4=0.36$	-	0.93-0.94-0.99
D ₁ + v_{CH}	-	-	0.27	
D ₁ + $v_{CH} + v_{ob}$ (3924 cm ⁻¹)	-	$\beta_2=0.72, \beta_4=0.5$	-	
D ₁ + $v_{CH} + v_{CC}$ (4466 cm ⁻¹)	-	-	-	0.82-0.83-0.85
D ₂	0.14	-	-	0.3-0.32-0.4

at 0.13 eV agrees well with D₂+ v_{CC} (orange dashed vertical line). We do not assign this peak at 0.13 eV to a D₀ ionisation by 264.7nm+2×800 nm, as this would imply a vibrational energy of 260 meV (2096 cm⁻¹) which does not correspond to any of the vibrational cation modes calculated or detected^{31,32}. Similarly to the one-colour ionisation at 800 nm (Figure 4b), two colour photoionisation with an ultra-short (probe) pulse reveals vibrational activity.

As already discussed in Figure 4, we do not consider Rydberg fingerprints onto the D₀ continuum to be involved in the present TR-PES, despite the fact that the (s,p,d) Rydberg series have been calculated to lie between 5.2-6.36 eV³⁵. If these Rydberg states were populated at ~6.3 eV, their fingerprints would be expected at 0.91 eV for the s-Rydberg state, between 1.2 and 1.3 eV for the p-states, and finally between 1.6 and 2.06 eV for the d-ones, for a total ionisation energy of 9.33 eV.

In order to extract time dependencies of the background-subtracted-TRPES in Figure 5a, different kinetic energy ranges were integrated (as marked by transparent, coloured energy areas): around D₂ + v_{CC} (0.13 eV-orange); around D₁ - v_{CH} + v_{CC} (0.52 eV-green); around D₁ + v_{CC} (0.9 eV-light blue); and finally around D₀ ($n = 3, 1.5$ eV-dark blue). These four areas were subsequently compared to the time-dependency of the tail of the PES integrated between 2 and 7 eV. The transients of these five integrations, normalised by their respective energy ranges, are shown in Figure 5d (*i.e.* integration of Figure 5a). The transients are then background corrected by subtracting the contribution at 10 ps, as shown in Figure 5e (*i.e.* integration of Figure 5b). The three first peaks' components, all containing vibrational activity, increase up to 150 fs – very similarly to the C₆H₁₀⁺ transient shown in Figure 3a – and then decay (orange, green, light blue lines), while the PES with a kinetic energy larger than 1 eV simply decays during the cross-correlation time before rising very slightly. Table 2 summarises the time-constants extracted from these attempted fits.

4 *Ab initio* CALCULATIONS

In order to understand the propensity rule of photoionisation that drives both the one-color photoelectron intensities (Figure 4) and the time-resolved PES (Figure 5), we have carried out *ab initio* calculations.

The calculated singlet states are labelled a,b,c, etc. in increasing energy order in each symmetry.

Computational details: The geometry optimisations were performed without symmetry constraints at the DFT or TD-DFT levels using the B3LYP functional³⁶, in conjunction with the 6-31+G* basis set³⁷⁻³⁹ as available in the Q-Chem package⁴⁰. All the final geometries were found to belong to the D_{2h} symmetry point group. These calculations were complemented by the calculation of the harmonic frequencies to check that real minima were obtained. The geometry coordinates and the different C-C distances can be found in ESI†(Table S 1 and S 2). Using the geometry obtained for the ground state, correlated multireference (MR) wavefunction (WF) calculations were performed to obtain the electronic energies of the excited states of interest for neutral pyrene, and also for the lowest energy states of the cation and the dication. The MRWF calculations of the different states were carried out with the 7.8 MOLCAS package⁴¹⁻⁴³. They are based on Atomic Natural Orbitals⁴⁴. The (14s9p4d3f) primitive set was contracted to [4s3p2d] for the carbon atoms and the (8s4p3d) primitive set for the H atoms was contracted to [2s1p]. The Cholesky decomposition technique,^{45,46} was used with a 10⁻⁶ a.u. threshold. The calculations were performed in the D_{2h} symmetry group. The zeroth-order description was obtained by means of complete active space self-consistent field (CASSCF) calculations.⁴⁷ The active space contained 16 electrons in 16 orbitals (CAS(16,16)) corresponding to all the π orbitals. These orbitals belonged to the B_{3u}, B_{1g}, B_{2g}, and A_u symmetries, leading to states of A_g, B_{2u}, B_{1u}, and B_{3g} symmetries, in the orientation given in Figure-1(a). State average calculations were performed with 20 roots in A_g symmetry and 14, 18, 16 for the B_{2u}, B_{1u}, and B_{3g} symmetries. This number of roots allows access to CASSCF excitation energies up to 10 eV. Dynamical correlation effects were then included at the MS-CASPT2 level^{48,49}, where all the electrons were correlated. The real level shift was applied (0.5 a.u) to avoid intruder states. The Ionisation Potential-Electron Affinity (IPEA) shift⁵⁰ was not used, as it is often questioned⁵¹⁻⁵⁹. The number of roots calculated at the MS-CASPT2 level is 9 for each symmetry. The oscillator strengths were calculated thanks to the restricted active space state interaction approach (RASSI).⁶⁰ In addition to the singlet excited states, the first three doublet states corresponding to the cation, as well as the doubly ionised species, singlet states of A_g and B_{3g} symmetries, were also calculated. The

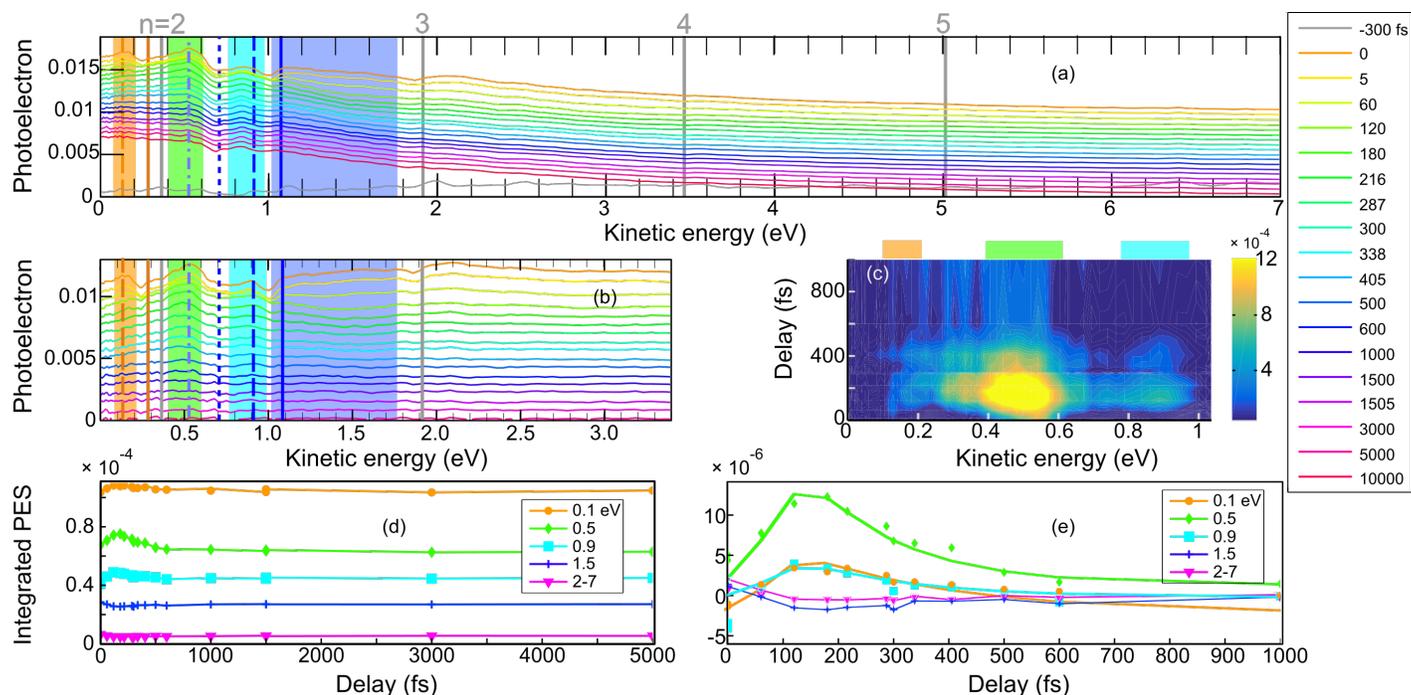


Fig. 5 Time resolved photoelectron spectra (TR-PES) recorded via 12 delay scans with images corresponding to 100 ms \times 50 recording time and the following sequence: 2 images with the pump pulse alone (10k laser shots) + 8 images in the pump-probe configuration (40k laser shots) + 2 images with the probe pulse alone (10k laser shots), in order to get a proper statistic on the subtraction of the background resulting from pump alone and probe alone. The kinetic energy axis in panels (a) and (b), calibrated by rare gas photoelectron spectroscopy, has been down shifted by 65 meV to correct for the ponderomotive shift induced by the 800 nm probe pulse. We present (a) TR-PES as a function of kinetic energy, where the vertical lines in grey are the ATI limits on the D_0 threshold ($\hbar\nu_{pump} + n \times \hbar\nu_{probe} - D_0$); the blue lines (reached with $n=3$) mark the D_1 continuum, e.g. with the origin band, the CC stretching at 1389 cm^{-1} , the CH stretching at 3077 cm^{-1} and a combination of CH and CC stretching modes at 4466 cm^{-1} ; and the orange lines, the D_2 continuum with its threshold and the CC stretching. In panel (b), the PES is subtracted from the PES recorded at 10 ps pump-probe delay to enhance the visibility of the time dependency of the vibrational activities. The same colour code as in Figure 5a is used for the delays and the vertical lines. Panel (c) shows a contour map representation of the data shown in (b). Panel (d) presents an integration of the PES over the energy ranges highlighted in (a), and compared to the PES integrated from 2 to 7 eV. Panel (e) presents the same integration as in (d), but instead performed on the PES presented in (b) *i.e.* 10 ps PES-subtracted data. The time constants extracted from the attempted fits of figure 5e are listed in Table 2.

three doublet states differ by the nature of the mono-occupied orbital: when the mono-occupied orbital corresponds to the Highest Occupied Molecular Orbital (HOMO) in the neutral species, the doublet state is called D_0 . In the same way, the two others (D_1 and D_2) correspond to a hole in the HOMO-1 (D_1) and HOMO-2 (D_2) orbitals.

Results: The occupied and virtual molecular orbitals obtained at the CASSCF level are given in the ESI†(Figure S3). Their shapes illustrate the relevance of the Mirror Theorem^{61,62} which establishes one to one correspondence of the amplitudes between H- and L+*i* MOs with a change of the phases of one atom over two. The HOMO (H) / LUMO (L) denomination corresponds to the DFT orbital energies. The vertical excitation energies, the oscillator strengths from the ground state, and the electronic configurations of the excited states are presented in Table 4. The allowed transitions correspond to excited states of $B_{2u}(y)$ and $B_{1u}(z)$ symmetries. Below the S_3 (calculated at 4.44 eV) state, three allowed states are found. The first excited state aB_{2u} at 3.43 eV has a very small oscillator strength. Two states, aB_{1u} (3.82 eV) and bB_{2u} (4.44 eV) present significant oscillator strengths (0.38 and 0.48 respectively). It is this latter state in which a wavepacket is created at $t=0$ fs. The agreement with experimental values is excellent for the aB_{2u} (3.43 eV for 3.34-3.42 eV) and aB_{1u} (3.82 eV for 3.65-3.85 eV) states. The bB_{2u} (4.44 eV for 4.55-4.69 eV) is not so close, although it is still within the standard error of MS-CASPT2 calculations (≈ 0.2 eV). Higher states are also in good agreement with the experimental values, with differences of between 0.04 and 0.24 eV compared to the values derived from the one and two-photon spectroscopies. One can note that the calculations are performed in the geometry of the ground state, which may explain the overestimation of some calculated values as in the case of the bB_{3g} and the cB_{3g} states. As the bB_{2u} , the bB_{3g} and the aB_{2u} states are essential in explaining the electronic relaxations observed, their respective geometries were optimised. Although the geometry of the S_3 - bB_{2u} state is only slightly different from the ground state geometry, the three central CC distances parallel or along the *z* axis of the bB_{3g} state geometry are lengthened (4.3% on the *z* axis and 3.2% for the two others). In their respective geometries, the bB_{3g} CASPT2 energy is found lower than the bB_{2u} one, in agreement with the experimental values⁶³. Furthermore, the optimisation of the minimum-energy crossing point connecting the two states was performed, followed by the determination of the non adiabatic coupling vector at this point, which is found to be non zero (see ESI Table S 3).

Oscillator strengths larger than 0.01 between excited states are presented in ESI†-Table S 4. These oscillator strengths are, as expected, small. The two largest values (0.15 and 0.13) correspond to transitions from the aB_{1u} to the gA_g states and from aB_{2u} to the fB_{3g} states. However, these two transitions are not involved in the experimental process since the polarisations of both lasers are parallel (*y*-orientated dipole), therefore, only transitions with B_{2u} character will be induced, *i.e.*, transitions between states of symmetries B_{1u} and B_{3g} , or B_{2u} and A_g . Concerning the ionised species (See Table 1), for the cations, the calculated values differ only by at most 0.03 eV from the experimental values. Two dications were calculated, the lowest one (A_g), at 19.24 eV, cor-

responds to a double hole in the HOMO orbital while the second one (B_{3g}), at 19.86 eV corresponds to one hole in the HOMO and one in the HOMO-1. The experimental value measured by Threshold- PEPICO in the VUV range is 19.8 ± 0.2 eV²².

5 DISCUSSION

The pump pulse excites the second bB_{2u} state of pyrene, commonly called the S_3 state. As expected from its main electronic configuration shown in Table 4, the one-photon ionisation from this state will populate with roughly equal propensity the D_0 ground state of the cation at 46 % and D_1 at 54 % – with percentages obtained by normalising the 30 and 35 % values calculated. We also calculated the Dyson orbitals and their norms to confirm this assessment (see Table S 5 in ESI†). The branching ratio measured in the one-colour UV PES (Figure 4a) is $38 \pm 9\%$ for D_0 and $62 \pm 12\%$ for D_1 after re-normalisation of the values 31 % D_0 and 51 % D_1 extracted from the fit of the PES. This shows the same trend as the *ab initio* calculation. However, the $18 \pm 2\%$ yield observed for D_2 also reveals that, on a timescale shorter than the pump duration (~ 100 fs), the first internal conversion from the bB_{2u} state is already efficiently transferring the wavepacket amplitude to another electronic state with a D_2 character in photoionisation. Since this D_2 character was not observed in multiphoton ionisation – resonant with the bB_{2u} state – with a shorter pulse duration (800 nm - 25 fs), the lifetime of the bB_{2u} state has to be in the 25-100 fs range. By referring to Table 4, it is obvious that the only possible candidate with a very strong D_2 character (57 %) is the bB_{3g} state calculated at 4.53 eV, slightly above the bB_{2u} state at the equilibrium geometry of the ground state. From the pump-probe photoelectron yield onto D_2 (orange component in Figure 5e), we can deduce that this bB_{3g} state is populated within the first 80 fs ($t_0 = 80$ fs), before decaying electronically into lower energy electronic states in ~ 280 fs. From this attempted fit of the TR-PES(D_2), the lifetime of the bB_{2u} wavepacket prepared by the pump pulse, is around 80 fs. The vibrational modes that are expected to promote this first internal conversion are of b_{1u} symmetry, thus non-Franck-Condon active nuclear modes. Among the 72 vibrational modes of pyrene, the b_{1u} ones are expected to be two C-H stretches (around 3000 cm^{-1}), six C-H bend+C-C stretch (between 1000 and 1554 cm^{-1}), one C-H bend (around 1100 cm^{-1}) and one C-H bend+ring deformation (around 900 cm^{-1}) and finally two ring deformations⁶⁵. This 80 fs measurement is longer than the 20 fs lifetime deduced from the 34 meV absorption bandwidth (Figure 1a) assuming an homogeneous broadening due to the first internal conversion. Since the polarisations of both lasers are parallel (*y*-orientated dipole), the NIR will induce a transition with B_{2u} character. In this line of argument, the D_2 character of the bB_{3g} state could be enhanced in the multiphoton NIR ionisation by the intermediate resonance with the cB_{1u} state, calculated with a 50 % character of D_2 , at 6.05 eV with an oscillator strength $cB_{1u} \leftarrow bB_{3g}$ of 0.02. Once the population in the bB_{3g} state is zero, there is no way to photoionise into the D_2 cation state within the approximation of a frozen ionic core, as expected from the electronic configuration of the states lying at lower energy (Table 4).

Table 4 Excitation energies (eV) and oscillator strength from the ground state. Electronic configurations for excited states calculated with MS-CASPT2 at the equilibrium geometry of the ground electronic state. Only weights of the determinants above 7% are listed.

State	Energy	Oscillator strength	Main electronic configurations	Weight in %	Expected ionisation	Mono and Di excited character (%)	Exp in eV	Two-Photon exp in eV ⁶³
aB _{2u}	3.43	0.14E-03 (y)	H → L+1 H-1 → L	33 28	D ₀ D ₁	63 / 8	3.34 ⁶⁴ /3.37 ⁶⁵ /3.42 ⁶⁶	
aB _{1u}	3.82	0.38 (z)	H → L	66	D ₀	74 / 4	3.65 ¹⁵ / 3.71 ^{64,67} /3.85 ^{66,68}	
aB _{3g}	4.15	Not allowed	H → L+2	61	D ₀	64 / 10		4.12 (0-0) / 4.23
bB _{2u} (S ₃)	4.44	0.48 (y)	H-1 → L H → L+1	35 30	D ₁ D ₀	68 / 6	4.55 ^{64,67} /4.68 ^{66,68} /4.69 ¹⁵	
bA _g	4.47	Not allowed	H → L+3 H H → L L H-3 → L	19 16 17	D ₀	43 / 24		4.54 (0-0) / 4.61
bB _{3g}	4.53	Not allowed	H-2 → L	57	D ₂	65 / 10		4.29 (0-0)
cA _g	4.94	Not allowed	H-1 → L+2	45	D ₁	53 / 16		5.16 (0-0)
cB _{3g}	5.07	Not allowed	H-4 → L H → L+4 H-3 → L+1	19 10 9	D ₀	48 / 19		4.94 (0-0)
dA _g	5.09	Not allowed	H-2 → L+1	45	D ₂	58 / 12		
bB _{1u}	5.28	1.29 (z)	H-1 → L+1	62	D ₁	70 / 5	5.15 ⁶⁴ /5.17 ⁶⁷ /5.35 ⁶⁸ /5.36 ¹⁵ /5.40 ⁶⁶	
eA _g	5.41	Not allowed	H → L+3 H-3 → L	29 26	D ₀	70 / 2		
dB _{3g}	5.52	Not allowed	H-1 → L+3 H-3 → L+1	19 14	D ₁	42 / 25		
cB _{2u}	5.74	0.02 (y)	H-3 → L+2 H-2 → L+3	26 15	D ₂	43 / 19		
eB _{3g}	5.85	Not allowed	H-1 → L+3 H-3 → L+1 H H → L L+1 H → L+4	20 18 13 8	D ₁ D ₀	51 / 23		
dB _{2u}	5.86	0.78E-03 (y)	H-4 → L+3 H-3 → L+4 H H-4 → L L	11 7 9		21 / 40		
fA _g	6.04	Not allowed	H-1 H → L L+2 H-4 → L+1 H-1 → L+4	15 9 8	D ₁	22 / 42		
cB _{1u}	6.05	0.63 (z)	H-2 → L+2	50	D ₂	61 / 10		
dB _{1u}	6.26	0.04 (z)	H-5 → L H → L+5 H-3 H → L L	16 10 7	D ₀	29 / 34		
gA _g	6.36	Not allowed	H-1 H-1 → L+1 L+1 H-4 → L+1 H-1 → L+4 H H → L L	9 7 7 8	D ₁	15 / 48		

Table 4 Continued. Excitation energies (eV) and oscillator strength from the ground state. Electronic configurations for excited states calculated with MS-CASPT2 at the equilibrium geometry of the ground electronic state. Only weights of the determinants above 6% are listed.

State	Energy	Oscillator strength	Main electronic configurations	Weight in %	Expected ionisation	Mono and Di excited character (%)	Exp in eV	Two-Photon exp in eV ⁶³
eB _{2u}	6.40	0.009 (y)	H-6 → L H → L+6	19 7	D ₀	32 / 30		
fB _{2u}	6.63	1.072 (y)	H-2 → L+3 H-3 → L+2 H H-2 → L L H H → L+2 L	28 19 7 6	D ₂	49 / 19		
hA _g	6.69	Not allowed	H-1 H-1 → L+1 L+1	5		14 / 45		
fB _{3g}	6.72	Not allowed	H-1 H → L L H H → L+1 L H-1 H → L+1 L+1 H-1 H-1 → L+1 L	19 16 9 6		11 / 62		
eB _{1u}	6.75	0.009 (z)	H-4 → L+2 H-3 → L+3	21 9		40 / 23		
fB _{1u}	6.94	0.045 (z)	H-3 → L+3	40		49 / 18		
gB _{3g}	7.04	Not allowed	H-1 H → L L	7		7 / 52		
iA _g	7.14	Not allowed	H H-1 → L+1 L H H → L+1 L+1 H-1 H-1 → L L	20 6 6		2 / 54		
gB _{2u}	7.15	0.001 (y)	H H → L+2 L H H-2 → L L	9 7		13 / 44		
hB _{2u}	7.19	0.004 (y)	H-5 → L+1 H-1 → L+5	17 6	D ₁	24 / 37		
hB _{3g}	7.25	Not allowed	H-5 → L+2	14		25 / 30		
iB _{3g}	7.58	Not allowed	H-7 → L H-6 → L+3	15 6		28 / 30		
gB _{1u}	7.61	0.008 (z)	H H → L+1 L+2 H H-2 → L+1 L	6 6		9 / 48		
hB _{1u}	7.92	0.007 (z)	H-3 H-2 → L+2 L	6		7 / 49		
jA _g	7.92	Not allowed	H H-2 → L+2 L	14		6 / 46		
iB _{2u}	8.02	0.00006 (y)				5 / 47		

The vibrational activity detected in D₂ is 172 meV (Figure 5a) for a pump pulse creating a ~250 meV vibrational energy in bB_{2u}. This indicates that the bB_{3g} state has an equilibrium geometry different from the bB_{2u} state (especially along the CC coordinate that is detected via photoionisation).

This was confirmed by the geometry optimisation (ESI Tables S 1 and S 2). Besides, the CASPT2 adiabatic excitation energy of the bB_{3g} state was found to be lower than the bB_{2u} state in their equilibrium geometries. This is more in agreement with the two-photon spectroscopy performed in the liquid phase that found this bB_{3g} state lying at 4.29 eV⁶³. Furthermore, the non adiabatic coupling vector at the crossing point of these two states, different from zero (ESI Table S 3), tends to confirm the population transfer from the bB_{2u} state to the bB_{3g} one. We do not observe any rising photoelectron components after 300 fs, *i.e.* the PES recorded

at 600 fs is the same as that at 10 ps, differing only in intensity. The simplest explanation for this is that the electronic state populated from the bB_{3g} state via a second internal conversion is a long-lived state (>100 ps). There are two possible states: the ground electronic state, from which we anticipate a lower probability of ionisation due to the extra NIR probe photons required to reach the appropriate Franck-Condon windows (4.68 eV vibrational energy), but also the aB_{2u} state. Gudipati *et al.*⁶⁹ as well as Numata *et al.*¹⁵ have recorded almost all the electronic absorption spectrum of pyrene in matrices and in gas jet by recording the fluorescence yield from the first excited state S₁, an aB_{2u} state lying at 3.37 eV. It is generally agreed that this S₁ is a bottleneck step in the relaxation process taking place in pyrene. In the liquid phase, the lifetime of the aB_{2u} state has been measured to be in the range of 300 ns.⁷⁰ This second internal conversion from the bB_{3g} state would also be promoted by vibrational modes of b_{1u}

symmetry.

The main TR-PES components of Figure 5 are two vibrational activities in D_1 with a rising time of 80 fs similar to the D_2 component and a decay slightly shorter in the range of 200 fs. The similarity in the time-dependencies of TRPES(D_2) and TRPES(D_1) requires us to explore whether photoionisation of the bB_{3g} state can produce photoelectrons emitted in the D_1 continuum. With a D_1 weight of the bB_{3g} state at 3 %, we can consider that the bB_{3g} state doesn't have any propensity rule on itself to be strongly photoionised onto the D_1 state and consequently the intermediate resonances reached by the NIR probe pulse at 6.2 eV and 7.8 eV, have to significantly enhance this D_1 contribution. In addition, the photoionisation path has to be stronger than the D_1 weight of the bB_{2u} state populated by the pump pulse (namely 35 %), since both the TR-PES(D_1) and the pyrene cation signals are time-shifted, by 80 fs and 22 fs, respectively. With a B_{2u} character for the NIR dipole of transition, states of B_{1u} symmetry need to be considered around 5-6.5 eV as possible candidates to promote the D_1 continuum. Table 4 shows that the only state with a strong D_1 character of 62 % is the bB_{1u} state calculated at 5.28 eV. However, it should be noted here that the oscillator strength of the proposed NIR transition ($bB_{1u} \leftarrow bB_{3g}$) is relatively weak – $f = 0.002$ – and consequently enhancement by resonances reached around 7.8 eV in this 3 NIR-photons ionisation have to be strongly involved to compensate this first weak NIR transition. To summarise, there are two routes to photoionise the B_{3g} state: the first being a photoionisation into the D_2 state enhanced by a strongly electronically allowed resonance at 6.2 eV with the cB_{1u} state, and a second path onto the D_1 cation state by a weak transition with the bB_{1u} state that has to be significantly enhanced around 7.8 eV to get this ionisation path to be the strongest one. This is the simplest way to explain why, in Figure 5e, all the vibrational components present the same rising time and similar decays (as summarised in Table 2). The more complicated explanation is now to consider the states at lower energies or around the bB_{2u} state that have a strong D_1 character or a strong dipole of transition with the bB_{1u} state at 5.28 eV. There are no states with a strong dipole onto the bB_{1u} state (except the ground state). However the aB_{2u} state at 3.37 eV has a 28 % D_1 character that could be enhanced in the NIR multiphoton ionisation by A_g type resonances with a strong component of D_1 and a proper oscillator strength. Table 4 lists the cA_g (at 4.94 eV), the fA_g (at 6.04 eV) and the gA_g (at 6.36 eV) states with, respectively, 45%, 8%, and 7% D_1 weights. In line with this reasoning about the TRPES(D_1), the aB_{2u} - S_1 state could be populated in 80 fs by a vibronic coupling from the bB_{2u} state promoted by a_g vibrational Franck-Condon active modes and the 200 fs observed on the decay of the D_1 components would reveal the first moments of the intramolecular vibrational relaxation (IVR) in S_1 . In conclusion, there are two ways to populate the S_1 state: (i) a second internal conversion from the bB_{3g} state via b_{1u} promoting modes and (ii) a first vibronic coupling from the bB_{2u} state promoted by vibrational modes of a_g symmetry.

Since no clear vibrational components are observed after ~ 400 fs, we can also deduce that the NIR multiphoton ionisation into D_1 , from the aB_{2u} (S_1) state – populated by the second electronic coupling from the bB_{3g} state or directly, has a low

sensitivity to the vibrational energy. This is indeed expected since in this lower electronic state, the 1.23 eV vibrational energy will start to be dissipated into many different vibrational modes.

The similarity in the time-constants extracted from transients recorded on the $C_{16}H_{10}^+$ yield (Figure 3a/ Table 2) with those extracted for the D_1 and D_2 photoelectrons (Figure 5e /Table 2), leads us to conclude that the probability of NIR multiphoton ionisation from the bB_{3g} state is higher than the probability of photoionisation from the bB_{2u} state. Indeed, the Pyr^+ yield reaches a maximum at around 150 fs, similar to the D_1 and D_2 photoelectron peaks in Figure 5e. This 150 fs maximum encodes both the 22–80 fs lifetime of the bB_{2u} state as well as the 200 fs lifetime of the bB_{3g} state populated by electronic coupling. The proposed relaxation and the ionisation paths are all sketched in Figure 6. However what is not explained, is why the D_1 signature of the zero order state bB_{2u} prepared by the pump pulse, that is the strongest contribution at 2×264.7 nm (fig. 4a), does not contribute more significantly such that its trace will be visible on the pyrene cation transient and the TR-PES(D_1).

The mass spectrum that we present in Figure 2 is comparable to those previously recorded with slightly longer femtosecond pulses at higher intensities, including the large production of H^+ ²⁵. Based upon our photoelectron assignment, we will now discuss the transients in the ion spectra shown in Figure 3. The step contribution characterising the transient $C_{16}H_{10}^+$ signal for delays longer than 600 fs corresponds to the 1.23 eV vibrational wavepacket in the long-lived excited state aB_{2u} - S_1 . Indeed, the step amplitude reveals a significant probability of photoionisation that is more in agreement with a smaller vibrational energy and a smaller energy gap to reach the ionisation continuum than the ground state, for instance: two fewer NIR probe photons are required to reach the ion continuum from S_1 than from S_0 . The 318 fs decay measured for the H^+ transient reveals that a dissociative ionisation channel forming $C_{16}H_9 + H^+$ can be reached from the aB_{2u} - S_1 state, at least during the very first IVR moments and before a too effective redistribution dispersed the 1.23 eV vibrational energy over large numbers of internal degrees of freedom, preventing a poor nuclear overlap with the $C_{16}H_9 + H^+$ continuum. We rule out the possibility that the present pump probe experiment can detect the H neutral fragments eventually produced by the 20% of the pump pulse that lies above the 4.7 eV dissociation threshold¹⁶. Indeed, while it is easy to reach a molecular ion continuum above 13.6 eV thanks to the plethora of intermediate molecular resonances, ionising an atom by multiphoton transitions is much more challenging due to the low ionisation cross-section of H and the narrowness of the scarce resonances. However, it is clear that a UV excitation close to the H-dissociation threshold will start to efficiently populate vibrational modes associated with CH-stretch/bending modes. To explain the main contribution to the H^+ transient (centred around 0 fs, with a very short decay of 29 fs), another excitation path must be considered. The 18.3 eV threshold for H^+ production is easier to reach during the cross-correlation time than when the delay is longer than

50 fs. This H^+ component could therefore come from all possible photon combinations and thus not be directly associated with the dynamics triggered in the bB_{2u} - S_3 state by one photon of the pump pulse. Under the current experimental conditions, we cannot rule out a further possibility for the H^+ transient: signature of an electronically excited cation populated by 2×264.7 nm, with its relaxation dynamics projected onto the H^+ dissociative continuum by the NIR probe pulse. Figure 4a demonstrates that, on average, we can expect around 500 meV of vibrational energy in D_1 . However, this 500 meV does not seem high enough to explain the 318 fs decay observed on the H^+ transient and, on the contrary, this 2×264.7 nm pump path does certainly contribute to the H^+ step observed at long delay (>800 fs).

The formation of H_2^+ was also observed during this experiment (Figure 2), but its low yield prevented us from recording its time-transients. However, given that one of the motivations for studying PAHs is their astrophysical relevance, it is interesting to note that H^+ and H_2^+ are formed via different, competing, pathways during the photoionisation process of pyrene. Both of these species are of high importance in interstellar environments due to their role as intermediates in the formation and destruction of highly abundant species such as H_2 – the most abundant interstellar molecule⁷¹ – and H_3^+ – the most abundantly produced interstellar ion, that plays a key proton donor role and initiates ion-molecule hydrogenation reactions leading to the formation of complex molecules.⁷² In a more general context, it is relevant to address why so many protons are produced in the femtosecond regime of multiphoton ionisation (here, as well as in²⁵) and conversely almost never by multiply charged ions collision²⁸ or VUV photoionisation⁷. One line of investigation is to consider the temporal conditions of the dissociation ionisation channels¹⁴. It was found that cations created around 17-19 eV required 40 fs dynamics before the dissociative parts of the potential are accessed. If this timescale is still relevant at the ionisation energies involved here, this might explain why, with our 25 fs-long IR probe pulse, the H^+ continuum can be reached efficiently when an intense activity along the CH-bending and stretching modes has been promoted by the UV-pump pulse. In line with this last argument and contrary to H^+ , the carbon backbone fragmentation channels lying at $\sim <19$ eV are not significant contributions in our pump-probe experiment. This is similar to that observed in the VUV range⁷. In conclusion, UV excitation does not enhance these channels of ionisation and/or these channels are protected by fission barriers that prevent to observe any pump-probe transient at M^+ -(H or C_2H_2 or C_3H_3) with a 25 fs probe pulse¹⁹.

In the pump-probe excitation scheme, the resonance around 4.68 eV enhances the probability of reaching the doubly and triply charged continua, as shown in Figure 2, Figure 3b, and the ESI†(Figure S2). In the case of the dication, we could have assigned this enhancement to a relaxation decay taking place from the bB_{2u} into the bA_g state calculated at 4.52 eV with a 17 % doubly excited character (HOMO,HOMO). Indeed, a population in a two-hole state (like bA_g), once projected onto the ionisation continuum – assuming the energy threshold (19.8 eV) is reached – could enhance the formation of a dication. The 45 fs decay ob-

served on the dication signal (Figure 3b) would thus not reflect the bB_{2u} - bA_g vibronic coupling, but rather the bA_g lifetime. Were this the case, a $t_0 \sim 22$ –80 fs should have been observed for this $C_{16}H_{10}^{2+}$ transient, to take into account the bB_{2u} lifetime. As this time-shift was not observed, this hypothesis is rejected. Another simpler explanation is that two hole state(s) are involved in the NIR multi-photon ionisation of the bB_{2u} state. This would then assign the observed decay of 45 fs to the bB_{2u} lifetime, which would match well with the previously assigned lifetime range of 22–80 fs extracted from the pyrene and the TR-PES (orange/cyan/green components) time-shifts t_0 . At 6.2 eV ($1+1'$), due to the polarisation constraint of the lasers, the states with A_g symmetry need to be taken into account for an enhanced multiphoton NIR ionisation, while at 7.78 eV it's the B_{2u} symmetry that must be considered. The fA_g (at 6.04 eV) and the gA_g (at 6.36 eV) states with a 42% and 48% total double hole configurations, respectively, are both good candidates. However their oscillator strengths from bB_{2u} are very weak with $f=0.0001$ and 0.006, respectively. The possibility of populating a double hole state at 6.2 eV needs to be enhanced by the states populated at ~ 7.8 eV with a B_{2u} symmetry. We found one at 7.15 eV with 44% doubly excited character and another one at 8 eV with a total of 47% doubly excited character to be the most likely candidates (see Table 4). Besides, we propose that, similarly to the H^+ step, the $C_{16}H_{10}^{2+}$ step at long delay results from the NIR double photoionisation of Pyr^+ cations created at 2×264.7 nm.

The third possible assignment of the Pyr^{2+} transient is a Pyr^+ wavepacket initiated at 3×264.7 nm and probed by projecting its dynamics onto the Pyr^{2+} continuum. Figure 4a shows that three photon ionisation corresponds to $30 \pm 10\%$ of the PES produced by the UV alone. In that case, we have few Pyr^+ that are created above 11.5-14 eV. As calculated by Mallocci *et al.*,⁷³ and as experimentally observed at 17 eV¹⁴, non-adiabatic relaxation in the cation at this energy range, probed by photoionisation, shows a transient on the dication with a decay of 37 fs. Being at lower energy in our case, we would expect a slower dynamic for the same process, thus explaining the ~ 45 fs decay in our experiment. Nonetheless, we submit that the first hypothesis (two hole state reached via NIR photoionisation) is the most likely. Indeed no step was observed on the dication signal formed by XUV+IR ionisation, on the contrary to what we observe in Figure 3b. In this context, it is difficult to rationalise a step at long delay resulting from 2×264.7 nm that would be only 75% less intense than a signal created at 3×264.7 nm around 0 fs.

We have presented here the simplest assignment that merges most of the temporal shifts and decays measured in the present pump-probe experiment. It is mainly the t_0 of Pyr^+ (22fs) and of TRPES (80fs), confirmed by the decay of Pyr^{2+} (45fs) that reveal the first internal conversion. Within the approximation of the frozen ionic core and without taking into account the Franck-Condon factors and nuclear dynamics, we can assign this population transfer to two possible states: (i) the bB_{3g} state populated by an internal conversion to justify the D_2 photoionisation and (ii) the long lived aB_{2u} state populated by a vibronic coupling. The Pyr^+ decay is then associated to (i) a second internal conversion from bB_{3g} state onto the aB_{2u} state or (ii) to IVR taking

place in the aB_{2u} state. We propose that the H^+ decay reveals the first moments of the IVR. This is the simplest conclusion that can be drawn from the recorded time-dependencies and it is not yet clear which of these two relaxation mechanisms is the dominant one.

6 CONCLUSIONS

We report in this article the first gas phase study of the ultrafast relaxation of electronic excitation taking place in cold pyrene. Electronic propensity rules, in combination with multiphoton-ionisation at the thresholds of the D_1 and D_2 ion continua, reveal all the electronic relaxations at play following the S_3 - bB_{2u} excitation. Due to the proximity to the cation thresholds, CC and CH stretching modes do appear in the photoionisation of the intermediate states bB_{3g} and aB_{2u} populated in 22-45-80 fs from the S_3 state. The dark bB_{3g} state, revealed by photoionisation onto the D_2 state, then decays onto the aB_{2u} long lived state in 200-280 fs. As the D_0 state is energetically accessible without any drastic electronic or vibrational conditions, the PES associated with this state is not really informative.

Final confirmation awaits the availability of a pump-probe experiment combined with an ion-electron coincidence with a very high rep. rate laser⁷⁴. This will allow the collection of the photoelectron spectra of all the ion species produced, but also the recording of the TR-PES as a function of the relative angle between the pump and probe polarisations in order to tune the propensity rules of NIR-probe multiphoton ionisation. A non-chirped UV pump pulse would also be required to resolve such fast dynamics. Multiphoton ionisation does introduce more constraints in the ionisation step and, as such, can enhance the sensitivity of pump-probe experiments. Another parameter that has been scarcely explored in such a peculiar probe step is the duration of the probe pulse. With post-compression modules and high repetition rate lasers now commercially available, such extensive studies can be envisioned. Combined with a fs-XUV pump-probe experiment, this will make the dissociative ionisation continuum a fully understood template for dynamics initiated in neutral molecules. Future experiments will extend the present study to the second and third bands of the S_3 state, and finally to compare the relaxation dynamics to even larger PAHs as well as catacondensed ones.

7 ACKNOWLEDGMENTS

This work was financially supported by Université de Bordeaux, the French programme national PCMI of CNRS/INSU with INC/INP co-funded by CEA and CNES PCMI-CNRS, the French research network EMIE GDR 3533 of CNRS and the agence nationale de la recherche, project PARCS ANR-13-S08-0005. The authors thank R. Bouillaud and L. Merzeau for their technical assistance. J.A.N. acknowledges the financial support of Horiba Scientific.

References

- 1 B. J. Finlayson-Pitts and J. N. Pitts, *Chemistry of the upper and lower atmosphere: theory, experiments, and applications*, Academic Press, San Diego, 2000.
- 2 Y. Carpentier, T. Pino and P. Bréchnignac, *J. Phys. Chem. A*, 2013, **117**, 10092–10104.
- 3 *The mechanisms of atmospheric oxidation of aromatic hydrocarbons*, ed. J. G. Calvert, Oxford University Press, Oxford ; New York, 2002.
- 4 C. Joblin, A. Léger and P. Martin, *Astrophys. J. Lett.*, 1992, **393**, L79–L82.
- 5 B. Draine, *Annu. Rev. Astron. Astrophys.*, 2003, **41**, 241–289.
- 6 A. G. G. M. Tielens, *Annu. Rev. Astron. Astrophys.*, 2008, **46**, 289–337.
- 7 J. Zhen, S. Rodriguez Castillo, C. Joblin, G. Mulas, H. Sabbah, A. Giuliani, L. Nahon, S. Martin, J.-P. Champeaux and P. M. Mayer, *Astroph. J.*, 2016, **822**, 113.
- 8 H. Andrews, A. Candian and A. G. G. M. Tielens, *Astron. Astrophys.*, 2016, **595**, A23.
- 9 A. M. Cook, A. Ricca, A. L. Mattioda, J. Bouwman, J. Roser, H. Linnartz, J. Bregman and L. J. Allamandola, *Astron. J.*, 2015, **799**, 14.
- 10 G. Mallocci, G. Mulas, C. Cecchi-Pestellini and C. Joblin, *Astron. Astrophys.*, 2008, **489**, 1183–1187.
- 11 G. C. Sloan, T. L. Hayward, L. J. Allamandola, J. D. Bregman, B. DeVito and D. M. Hudgins, *Astrophys. J. Lett.*, 1999, **513**, L65–L68.
- 12 H.-S. Kim, D. R. Wagner and R. J. Saykally, *Phys. Rev. Lett.*, 2001, **86**, 5691–5694.
- 13 V. Blanchet, K. Raffael, G. Turri, B. Chatel, B. Girard, I. Garcia, I. Wilkinson and B. Whitaker, *J. Chem. Phys.*, 2008, **128**, 164318.
- 14 A. Marciniak, V. Despré, T. Barillot, A. Rouzée, M. C. E. Galbraith, J. Klei, C.-H. Yang, C. T. L. Smeenk, V. Lorient, S. N. Reddy, A. G. G. M. Tielens, S. Mahapatra, A. I. Kuleff, M. J. J. Vrakking and F. Lépine, *Nat. Com.*, 2015, **6**, 7909.
- 15 Y. Numata, Y. Suzuki and I. Suzuka, *J. Photochem. Photobiol. A*, 2012, **237**, 49–52.
- 16 A. I. S. Holm, H. a. B. Johansson, H. Cederquist and H. Zettergren, *J. Chem. Phys.*, 2011, **134**, 044301.
- 17 A. Markevitch, S. Smith, D. Romanov, H. Bernhard Schlegel, M. Ivanov and R. Levis, *Phys. Rev. A*, 2003, **68**, 011402.
- 18 J. Zhen, D. Paardekooper, A. Candian, H. Linnartz and A. Tielens, *Chem. Phys. Lett.*, 2014, **592**, 211–216.
- 19 B. West, F. Useli-Bacchitta, H. Sabbah, V. Blanchet, A. Bodi, P. M. Mayer and C. Joblin, *J. Phys. Chem. A*, 2014, **118**, 7824–7831.
- 20 M. Gatchell, M. H. Stockett, N. de Ruelle, T. Chen, L. Giacomozzi, R. F. Nascimento, M. Wolf, E. K. Anderson, R. De-launay, V. Vizcaino, P. Rousseau, L. Adoui, B. A. Huber, H. T. Schmidt, H. Zettergren and H. Cederquist, *Phys. Rev. A*, 2015, **92**, year.
- 21 J. Zhang, F. Han and W. Kong, *J. Phys. Chem. A*, 2010, **114**, 11117–11124.
- 22 P. M. Mayer, V. Blanchet and C. Joblin, *J. Chem. Phys.*, 2011, **134**, 244312.
- 23 M. Vala, J. Szczepanski, F. Pauzat, O. Parisel, D. Talbi and Y. Ellinger, *J. Phys. Chem.*, 1994, **98**, 9187–9196.

- 24 N. Rusteika, K. B. Møller and T. I. Sølling, *Chem. Phys. Lett.*, 2008, **461**, 193–197.
- 25 L. Robson, K. Ledingham, A. Tasker, P. McKenna, T. McCanny, C. Kosmidis, D. Jaroszynski, D. Jones, R. Issac and S. Jamieson, *Chem. Phys. Lett.*, 2002, **360**, 382–389.
- 26 F. Gámez, A. R. Hortal, B. Martínez-Haya, J. Soltwisch and K. Dreisewerd, *J. Mass Spectrom.*, 2014, **49**, 1127–1138.
- 27 K. Fujiwara, A. Harada and J.-i. Aihara, *J. Mass Spectrom.*, 1996, **31**, 1216–1220.
- 28 A. Ławicki, A. I. S. Holm, P. Rousseau, M. Capron, R. Maissonny, S. Maclot, F. Seitz, H. A. B. Johansson, S. Rosén, H. T. Schmidt, H. Zettergren, B. Manil, L. Adoui, H. Cedergren and B. A. Huber, *Phys. Rev. A*, 2011, **83**, 022704.
- 29 M. S. Deleuze, *J. Chem. Phys.*, 2002, **116**, 7012–7026.
- 30 F. Negri and M. Z. Zgierski, *J. Chem. Phys.*, 1994, **100**, 1387–1399.
- 31 H.-S. Kim and R. J. Saykally, *Astrophys. J. Supp. Series*, 2002, **143**, 455–467.
- 32 S. R. Langhoff, *J. Phys. Chem.*, 1996, **100**, 2819–2841.
- 33 M. Naganathappa and A. Chaudhari, *Month. Not. Roy. Astron. Soc.*, 2012, **425**, 490–505.
- 34 M. Goto and K. Hansen, *Chem. Phys. Lett.*, 2012, **522**, 23–27.
- 35 E. Bohl, B. Mignolet, J. O. Johansson, F. Remacle and E. E. B. Campbell, *Phys. Chem. Chem. Phys.*, 2017, **19**, 24090–24099.
- 36 A. D. Becke, *J. Chem. Phys.*, 1993, **98**, 5648–5652.
- 37 W. J. Hehre, R. Ditchfield and J. A. Pople, *J. Chem. Phys.*, 1972, **56**, 2257–2261.
- 38 P. Hariharan and J. Pople, *Theoret. Chim. Acta*, 1973, **28**, 213.
- 39 T. Clark, J. Chandrasekhar, G. W. Spitznagel and P. V. R. Schleyer, *J. Comput. Chem.*, **4**, 294–301.
- 40 Y. Shao, Z. Gan, E. Epifanovsky, A. T. Gilbert, M. Wormit, J. Kussmann, A. W. Lange, A. Behn, J. Deng, X. Feng, D. Ghosh, M. Goldey, P. R. Horn, L. D. Jacobson, I. Kaliman, R. Z. Khaliullin, T. Kus, A. Landau, J. Liu, E. I. Proynov, Y. M. Rhee, R. M. Richard, M. A. Rohrdanz, R. P. Steele, E. J. Sundstrom, H. L. W. III, P. M. Zimmerman, D. Zuev, B. Albrecht, E. Alguire, B. Austin, G. J. O. Beran, Y. A. Bernard, E. Berquist, K. Brandhorst, K. B. Bravaya, S. T. Brown, D. Casanova, C.-M. Chang, Y. Chen, S. H. Chien, K. D. Closser, D. L. Crittenden, M. Diedenhofen, R. A. D. Jr., H. Do, A. D. Dutoi, R. G. Edgar, S. Fatehi, L. Fusti-Molnar, A. Ghysels, A. Golubeva-Zadorozhnaya, J. Gomes, M. W. Hanson-Heine, P. H. Harbach, A. W. Hauser, E. G. Hohenstein, Z. C. Holden, T.-C. Jagau, H. Ji, B. Kaduk, K. Khistyayev, J. Kim, J. Kim, R. A. King, P. Klunzinger, D. Kosenkov, T. Kowalczyk, C. M. Krauter, K. U. Lao, A. D. Laurent, K. V. Lawler, S. V. Levchenko, C. Y. Lin, F. Liu, E. Livshits, R. C. Lochan, A. Luenser, P. Manohar, S. F. Manzer, S.-P. Mao, N. Mardirossian, A. V. Marenich, S. A. Maurer, N. J. Mayhall, E. Neuscamman, C. M. Oana, R. Olivares-Amaya, D. P. O'Neill, J. A. Parkhill, T. M. Perrine, R. Peverati, A. Prociuk, D. R. Rehn, E. Rosta, N. J. Russ, S. M. Sharada, S. Sharma, D. W. Small, A. Sodt, T. Stein, D. Stück, Y.-C. Su, A. J. Thom, T. Tsuchimochi, V. Vanovschi, L. Vogt, O. Vydrov, T. Wang, M. A. Watson, J. Wenzel, A. White, C. F. Williams, J. Yang, S. Yeganeh, S. R. Yost, Z.-Q. You, I. Y. Zhang, X. Zhang, Y. Zhao, B. R. Brooks, G. K. Chan, D. M. Chipman, C. J. Cramer, W. A. G. III, M. S. Gordon, W. J. Hehre, A. Klamt, H. F. S. III, M. W. Schmidt, C. D. Sherrill, D. G. Truhlar, A. Warshel, X. Xu, A. Aspuru-Guzik, R. Baer, A. T. Bell, N. A. Besley, J.-D. Chai, A. Dreuw, B. D. Dunietz, T. R. Furlani, S. R. Gwaltney, C.-P. Hsu, Y. Jung, J. Kong, D. S. Lambrecht, W. Liang, C. Ochsenfeld, V. A. Rassolov, L. V. Slipchenko, J. E. Subotnik, T. V. Voorhis, J. M. Herbert, A. I. Krylov, P. M. Gill and M. Head-Gordon, *Molecular Physics*, 2015, **113**, 184–215.
- 41 F. Aquilante, L. De Vico, N. Ferré, G. Ghigo, P.-Å. Malmqvist, P. Neogrady, T. B. Pedersen, M. Pitoňák, M. Reiher, B. O. Roos, L. Serrano-Andrés, M. Urban, V. Veryazov and R. Lindh, *J. Comput. Chem.*, 2010, **31**, 224–247.
- 42 V. Veryazov, P.-O. Widmark, L. Serrano-Andrés, R. Lindh and B. O. Roos, *Int. J. Quantum Chem.*, 2004, **100**, 626–635.
- 43 G. Karlström, R. Lindh, P.-Å. Malmqvist, B. O. Roos, U. Ryde, V. Veryazov, P.-O. Widmark, M. Cossi, B. Schimmelpfennig, P. Neogrady and L. Seijo, *Comput. Mat. Science*, 2003, **28**, 222–239.
- 44 P.-O. Widmark, P.-Å. Malmqvist and B. O. Roos, *Theor. Chim. Acta*, 1990, **77**, 291–306.
- 45 F. Aquilante, T. B. Pedersen and R. Lindh, *J. Chem. Phys.*, 2007, **126**, 194106.
- 46 F. Aquilante, P.-Å. Malmqvist, T. B. Pedersen, A. Ghosh and B. O. Roos, *J. Chem. Theory Comput.*, 2008, **4**, 694–702.
- 47 B. O. Roos, P. R. Taylor and P. E. Siegbahn, *Chem. Phys.*, 1980, **48**, 157–173.
- 48 K. Andersson, P.-Å. Malmqvist, B. O. Roos, A. J. Sadlej and K. Wolinski, *J. Phys. Chem.*, 1990, **94**, 5483–5488.
- 49 J. Finley, P.-Å. Malmqvist, B. O. Roos and L. Serrano-Andrés, *Chem. Phys. Lett.*, 1998, **288**, 299–306.
- 50 G. Ghigo, B. O. Roos and P.-Å. Malmqvist, *Chem. Phys. Lett.*, 2004, **396**, 142–149.
- 51 A. Kerridge, *Phys. Chem. Chem. Phys.*, 2013, **15**, 2197–2209.
- 52 S. Vela, M. Fumanal, J. Ribas-Arino and V. Robert, *J. Comput. Chem.*, 2016, **37**, 947–953.
- 53 M. Kepenekian, V. Robert and B. Le Guennic, *J. Chem. Phys.*, 2009, **131**, 114702.
- 54 R. Mariusz, P. Rejmak, M. Fitta, M. Balanda and J. Szklarzewicz, *Phys. Chem. Chem. Phys.*, 2015, **17**, 14890–14902.
- 55 F. Ruipérez, F. Aquilante, J. M. Ugalde and I. Infante, *J. Chem. Theory Comput.*, 2011, **7**, 1640–1646.
- 56 S. Vancoillie, P.-Å. Malmqvist and V. Veryazov, *J. Chem. Theory Comput.*, 2016, **12**, 1647–1655.
- 57 J. P. Zobel, J. J. Nogueira and L. Gonzalez, *Chem. Sci.*, 2017, **8**, 1482–1499.
- 58 C. Wiebeler, V. Borin, A. V. Sanchez de Arano, I. Schapiro and A. C. Borin, *Photochem. Photobiol.*, 2017, **93**, 888–902.
- 59 N. Ben Amor, A. Soupart and M.-C. Heitz, *J. Mol. Mod.*, 2017, **23**, 23–53.
- 60 P.-Å. Malmqvist, B. O. Roos and B. Schimmelpfennig, *Chem. Phys. Lett.*, 2002, **357**, 230–240.
- 61 H. C. Longuet-Higgins, *J. Chem. Phys.*, 1950, **18**, 265–274.

- 62 G. G. Hall, *Proc. of the Royal Society A: Mathematical, Physical and Engineering Sciences*, 1955, **229**, 251–259.
- 63 P. Salvi, P. Foggi and E. Castellucci, *Chem. Phys. Lett.*, 1983, **98**, 206–211.
- 64 *DMS UV Atlas of Organic Compounds*, Verlag Chemie, Weinheim, and Butterworths, London.
- 65 M. Baba, M. Saitoh, Y. Kowaka, K. Taguma, K. Yoshida, Y. Semba, S. Kasahara, T. Yamanaka, Y. Ohshima, Y.-C. Hsu and S. H. Lin, *J. Chem. Phys.*, 2009, **131**, 224318.
- 66 R. S. Becker, I. S. Singh and E. A. Jackson, *J. Chem. Phys.*, 1963, **38**, 2144–2171.
- 67 C. M. Jones and S. A. Asher, *J. Chem. Phys.*, 1988, **89**, 2649–2661.
- 68 A. Thöny and M. J. Rossi, *J. Photochem. Photobiol A*, 1997, **104**, 25–33.
- 69 M. S. Gudipati, J. Daverkausen and G. Hohlneicher, *Chem. Phys.*, 1993, **173**, 143–157.
- 70 E. A. Mangle and M. R. Topp, *J. Phys. Chem.*, 1986, **90**, 802–807.
- 71 S. Cazaux and M. Spaans, *Astron. Astrophys.*, 2009, **496**, 365–374.
- 72 T. Oka, *Proc. Natl. Acad. Sci.*, 2006, **103**, 12235–12242.
- 73 G. Mallocci, G. Cappellini, G. Mulas and A. Mattoni, *Chem. Phys.*, 2011, **384**, 19–27.
- 74 A. Comby, E. Bloch, C. Bond, D. Descamps, J. Miles, S. Petit, S. Rozen, J. Greenwood, V. Blanchet and Y. Mairesse, *Nat. Com.*, 2018, **9**, 5212.